Accurate inspiral-merger-ringdown gravitational waveforms for nonspinning black-hole binaries including the effect of subdominant modes

Ajit Kumar Mehta,[1] Chandra Kant Mishra,[1,2] Vijay Varma,[3,1] and Parameswaran Ajith[1,4]

[1]International Centre for Theoretical Sciences, Tata Institute of Fundamental Research,
Bangalore 560012, India
[2]Indian Institute of Technology Madras, Chennai 600036, India
[3]Theoretical Astrophysics, California Institute of Technology, 350-17, Pasadena, California 91125, USA
[4]Canadian Institute for Advanced Research, CIFAR Azrieli Global Scholar, MaRS Centre, West Tower,
661 University Avenue, Suite 505, Toronto, Ontario M5G 1M1, Canada

We present an analytical waveform family describing gravitational waves (GWs) from the inspiral, merger, and ringdown of nonspinning black-hole binaries including the effect of several nonquadrupole modes [$(\ell = 2, m = \pm 1), (\ell = 3, m = \pm 3), (\ell = 4, m = \pm 4)$ apart from $(\ell = 2, m = \pm 2)$]. We first construct spin-weighted spherical harmonics modes of *hybrid* waveforms by matching numerical-relativity simulations (with mass ratio 1–10) describing the late inspiral, merger, and ringdown of the binary with post-Newtonian/effective-one-body waveforms describing the early inspiral. An analytical waveform family is constructed in frequency domain by modeling the Fourier transform of the hybrid waveforms making use of analytical functions inspired by perturbative calculations. The resulting highly accurate, ready-to-use waveforms are highly faithful (unfaithfulness $\simeq 10^{-4}$–10^{-2}) for observation of GWs from nonspinning black-hole binaries and are extremely inexpensive to generate.

I. INTRODUCTION

LIGO's recent observations of gravitational waves (GWs) from coalescing binary black hole systems [1–3] mark the beginning of a new branch of astronomy. Based on the observed rate of GW signals, a large number of merger events can be expected in upcoming observing runs of Advanced LIGO and Virgo [4,5], providing us a unique opportunity to constrain the mass and spin distribution of binary black holes, to infer their astrophysical formation channels, and to probe the true nature of extreme gravity.

The most sensitive GW detection pipelines use the technique of matched filtering to detect GW signals from binary black holes [6,7], which involves cross-correlating the data with theoretical templates of expected signals. Post detection, the physical and astrophysical properties of the GW source are inferred by comparing the data with theoretical signal templates, by means of Bayesian inference [8]. Tests of general relativity (GR) using GW observations also involve comparing the data with GR templates to investigate the consistency of the observation with the prediction of GR [9]. Thus, accurate theoretical models of the expected signals are an essential input for GW astronomy.

Theoretical templates describing the gravitational waveforms from the inspiral, merger, and ringdown of binary black holes have been computed in recent years by combining perturbative calculations in GR with large-scale numerical relativity simulations [10–25]. Most of these waveform families aim to model only the leading (quadrupole; $\ell = 2, m = \pm 2$) modes of the gravitational radiation. Indeed, careful investigations suggest that the systematic errors introduced by neglecting subdominant (nonquadrupole) modes in the parameter estimation of the LIGO events are negligible [26]. Due to the near "face-on" orientations of the binaries and moderate mass ratios, the effect of subdominant modes was negligible in the observed signals—the systematic errors introduced by neglecting the subdominant modes were well within the statistical errors [26]. However, for binaries with large mass ratios or high inclination angles or large signal-to-noise ratios, the systematic errors can dominate the statistical errors, biasing our inference of the physical and astrophysical properties of the source (see, e.g., [27–29]). In addition, including the effect of subdominant modes can improve the precision with which source parameters can be extracted, due to the increased information content in the templates (see, e.g., [30–37]), potentially improving the accuracy of various observational tests of GR [38,39].

In this paper, we present an analytical waveform family describing GW signals from the inspiral, merger and ringdown of nonspinning black-hole binaries. These waveforms are constructed by combining perturbative calculations in GR with numerical-relativity (NR) waveforms in the "phenomenological" approach presented in a series of papers [20–25,40–42]. This frequency domain, closed form waveform family has excellent agreement (faithfulness >0.99) with "target" waveforms, including subdominant modes, for binaries with mass ratio up to 10. Target waveforms including subdominant modes (with $\ell \leq 4$, $m \neq 0$) have been constructed by matching NR simulations describing the late inspiral, merger and ringdown of the binary

with post-Newtonian (PN)/effective-one-body waveforms describing the early inspiral. Our highly accurate, ready-to-use, analytical waveforms are both effectual and faithful for observation of GWs from nonspinning black-hole binaries and are extremely inexpensive to generate.

This paper is organized as follows: Section II presents the construction of the analytical inspiral, merger, ringdown waveforms by combining numerical relativity with perturbative calculations in general relativity. In particular, Sec. II A describes the construction of hybrid waveforms by matching the spherical harmonic modes of PN and NR waveforms, while Sec. II B describes the construction of the analytical waveform family approximating these hybrid waveforms in the frequency domain. The faithfulness of the new analytical waveforms to the original hybrids is studied in Sec. II C. Section III presents some concluding remarks and discusses our future work. Supplementary calculations and information are presented in the Appendix.

II. THE WAVEFORM MODEL

The two polarizations $h_+(t)$ and $h_\times(t)$ of GWs can be conveniently expressed as a complex waveform $\mathfrak{h}(t) := h_+(t) - ih_\times(t)$. It is convenient to expand this in terms of the spin -2 weighted spherical harmonics so that the radiation along any direction (ι, φ_0) in the source frame can be expressed as

$$\mathfrak{h}(t; \iota, \varphi_0) = \sum_{\ell=2}^{\infty} \sum_{m=-\ell}^{\ell} Y_{\ell m}^{-2}(\iota, \varphi_0) \mathfrak{h}_{\ell m}(t). \quad (2.1)$$

The spherical harmonic modes $\mathfrak{h}_{\ell m}(t)$ are purely functions of the intrinsic parameters of the system (such as the masses and spins of the binary), while all the angular dependence is captured by the spherical harmonic basis functions $Y_{\ell m}^{-2}(\iota, \varphi_0)$. Here, by convention, the polar angle ι is measured with respect to the orbital angular momentum of the binary. The leading contribution to $\mathfrak{h}(t; \iota, \varphi_0)$ comes from the quadrupolar ($\ell = 2, m = \pm 2$) modes. The relative contributions of various subdominant (nonquadrupole) modes depend on the symmetries of the system. For nonspinning binaries, it can be seen from the PN inspiral waveforms that the three subdominant modes with the largest amplitudes are $(\ell = 3, m = 3), (\ell = 4, m = 4)$ and $(\ell = 2, m = 1)$. This observation seems to hold through the merger regime (described by NR waveforms) as well. Thus, in this paper we focus on the modeling of these three subdominant modes, apart from the dominant quadrupole modes. Note that, due to the symmetry of nonspinning binaries, where the orbital motion is fully restricted to a fixed plane, the negative m modes are related to positive m modes by a complex conjugation. That is $h_{\ell-m} = (-)^\ell h_{\ell m}^*$ [43]. Also, the $m = 0$ modes are comprised of the nonlinear memory in the waveform, which has only negligible effect in GW detection and parameter estimation. It is also challenging to accurately extract this nonoscillatory signal

from NR simulations [44,45]. Thus, only $m > 0$ modes are considered in this paper.

A. Construction of hybrid waveforms

In this paper, we construct an analytical waveform family in the Fourier domain, that describes the three subdominant modes $(\ell m = 33, 44, 21)$ apart from the dominant 22 mode of the GW polarizations from nonspinning black-hole binaries. We start by constructing the spherical harmonic modes of *hybrid* waveforms by combining PN and NR waveforms in a region where both calculations are believed to be accurate.

PN inspiral waveforms, scaled to unit total mass and unit distance, can be written as

$$\mathfrak{h}_{\ell m}^{\text{PN}}(t) = 2\eta v^2 \sqrt{\frac{16\pi}{5}} H_{\ell m} e^{-im\varphi_{\text{orb}}(t)}, \quad (2.2)$$

where $\eta = m_1 m_2 / M^2$ is the symmetric mass ratio and $M = m_1 + m_2$ is the total mass of the binary, $v = (M\omega_{\text{orb}})^{1/3}$ is the PN expansion parameter, $\omega_{\text{orb}} = d\varphi_{\text{orb}}/dt$ is the orbital frequency and φ_{orb} is the orbital phase. The PN mode amplitudes $H_{\ell m}$ are currently computed up to 3PN[1] accuracy by [43,47–49] while the 3.5PN orbital phase $\varphi_{\text{orb}}(t)$ can be computed in the adiabatic approximation using inputs given in [50] and references therein.

In order to improve the accuracy of the inspiral waveforms, we compute the phase evolution of the inspiral part from the 22 modes of the effective-one-body (EOB) waveforms calibrated to NR simulations (SEOBNRv4 [13]). Hence, our inspiral waveforms are given by

$$\mathfrak{h}_{\ell m}^{\text{PN}}(t) = 2\eta v^2 \sqrt{\frac{16\pi}{5}} H_{\ell m} e^{-im\varphi_{\text{EOB22}}(t)/2}, \quad (2.3)$$

where φ_{EOB22} is the phase of the 22 mode of the SEOBNRv4 waveform. Note that, for $m = 2$ modes, $H_{\ell m}$ contains imaginary terms at order 2.5PN and above, which can be absorbed into the phase. However, since this correction appears at order 5PN and above in the phase, we neglect these corrections and use $|H_{\ell m}|$ instead of $H_{\ell m}$ for the $m = 2$ modes.

Hybrid waveforms containing all the relevant modes ($\ell \leq 4, 1 \leq m \leq \ell$) are constructed by matching NR modes $\mathfrak{h}_{\ell m}^{\text{NR}}(t)$ with PN modes $\mathfrak{h}_{\ell m}^{\text{PN}}(t)$ with the same intrinsic binary parameters. The PN waveforms are matched with NR by a least square fit over two rotations[2] on the NR

---

[1]The dominant, 22 mode inspiral model that we use here is actually 3.5PN accurate [46].

[2]These two rotations are necessary due to the freedom in choosing the frame with respect to which the NR and PN waveforms are decomposed into spherical harmonics modes. In general, three Euler rotations (ι, φ_0, ψ) can be performed between the two frames. However, one angle (ι) is fixed by the choice of aligning the z axis along the direction of the total angular momentum of the binary [27,51].

waveform and the time-difference between NR and PN waveforms over an appropriately chosen matching interval (t_1, t_2), where the NR and PN calculations are believed to be accurate.

$$\min_{t_0,\varphi_0,\psi} \int_{t_1}^{t_2} dt \sum_{\ell,m} |\mathfrak{h}_{\ell m}^{\mathrm{NR}}(t-t_0)e^{i(m\varphi_0+\psi)} - \mathfrak{h}_{\ell m}^{\mathrm{PN}}(t)|. \quad (2.4)$$

The hybrid waveforms are constructed by combining the NR waveform with the "best matched" PN waveform in the following way,

$$\mathfrak{h}_{\ell m}^{\mathrm{hyb}}(t) \equiv \tau(t)\mathfrak{h}_{\ell m}^{\mathrm{NR}}(t-t_0')e^{i(m\varphi_0'+\psi')} + [1-\tau(t)]\mathfrak{h}_{\ell m}^{\mathrm{PN}}(t), \quad (2.5)$$

where t_0', φ_0', and ψ' are the values of t_0, φ_0, and ψ that minimizes the difference δ between PN and NR waveforms. Above, $\tau(t)$ is a weighting function defined by

$$\tau(t) \equiv \begin{cases} 0 & \text{if } t < t_1 \\ \frac{t-t_1}{t_2-t_1} & \text{if } t_1 \le t < t_2 \\ 1 & \text{if } t_2 \le t. \end{cases} \quad (2.6)$$

Our hybrid waveforms include spherical harmonic modes up to $\ell = 4$ and $m = -\ell$ to ℓ in this analysis, except the $m = 0$ modes. We use a subset of these hybrid waveforms for constructing the analytical waveforms in the Fourier domain and to test the faithfulness of the analytical waveforms. The NR waveforms that were used to construct the hybrids are listed in Table I. Note that, although the analytical waveforms only model the 22,33,44,21 modes, their faithfulness is established by computing their mismatches with hybrids containing all the modes up to $\ell = 4$, except the $m = 0$ modes.

B. Construction of the analytical waveform model

In this section, we construct an analytical model for the Fourier transform $\mathfrak{h}_{\ell m}(f)$ of the real part of $\mathfrak{h}_{\ell m}(t)$ for the 22, 33, 44, 21 modes. Due to the symmetry of the nonspinning binaries, the Fourier transform of the imaginary part of $\mathfrak{h}_{\ell m}(t)$ can be computed by adding a phase shift of $\pi/2$ to $\mathfrak{h}_{\ell m}(f)$ (see Appendix C). Writing this in terms of a Fourier domain amplitude and phase

$$\mathfrak{h}_{\ell m}(f) = A_{\ell m}(f)e^{i\Psi_{\ell m}(f)}, \quad (2.7)$$

our phenomenological model for the amplitude of each mode is the following:

$$A_{\ell m}(f) = \begin{cases} A_{\ell m}^{\mathrm{IM}}(f); & f < f_{\ell m}^{\mathrm{A}} \\ A_{\ell m}^{\mathrm{RD}}(f); & f \ge f_{\ell m}^{\mathrm{A}}. \end{cases} \quad (2.8)$$

The Fourier frequencies below the matching frequency $f_{\ell m}^{\mathrm{A}}$ roughly correspond to the inspiral-merger stages of the

TABLE I. Summary of the parameters of the NR waveforms used in this paper: $q \equiv m_1/m_2$ is the mass ratio of the binary, $M\omega_{\mathrm{orb}}$ is the orbital frequency after the junk radiation and e is the residual eccentricity. The waveforms listed under the title "Fitting" are used to produce the analytical fits described in Sec. II B, while those listed under the title "Verification" are used for assessing the faithfulness of the analytical model in Sec. II C.

Simulation ID	q	$M\omega_{\mathrm{orb}}$	e	No of orbits
Fitting				
SXS:BBH:0198	1.20	0.015	2.0×10^{-4}	20.7
SXS:BBH:0201	2.32	0.016	1.4×10^{-4}	20.0
SXS:BBH:0200	3.27	0.017	4.1×10^{-4}	20.1
SXS:BBH:0182	4.00	0.020	6.8×10^{-5}	15.6
SXS:BBH:0297	6.50	0.021	5.9×10^{-5}	19.7
SXS:BBH:0063	8.00	0.019	2.8×10^{-4}	25.8
SXS:BBH:0301	9.00	0.023	5.7×10^{-5}	18.9
SXS:BBH:0185	9.99	0.021	2.9×10^{-4}	24.9
Verification				
SXS:BBH:0066	1.00	0.012	6.4×10^{-5}	28.1
SXS:BBH:0184	2.00	0.018	7.6×10^{-5}	15.6
SXS:BBH:0183	3.00	0.019	6.3×10^{-5}	15.6
SXS:BBH:0182	4.00	0.020	6.8×10^{-5}	15.6
SXS:BBH:0187	5.04	0.019	5.0×10^{-5}	19.2
SXS:BBH:0181	6.00	0.017	7.9×10^{-5}	26.5
SXS:BBH:0298	7.00	0.021	4.0×10^{-4}	19.7
SXS:BBH:0063	8.00	0.019	2.8×10^{-4}	25.8
SXS:BBH:0301	9.00	0.023	5.7×10^{-5}	18.9
SXS:BBH:0185	9.99	0.021	2.9×10^{-4}	24.9

signal, while the frequencies above $f_{\ell m}^{\mathrm{A}}$ roughly corresponds to the ringdown stage. The amplitude model for the inspiral-merger part is given by

$$A_{\ell m}^{\mathrm{IM}}(f) = A_{\ell m}^{\mathrm{PN}}(f)\left(1 + \sum_{k=0}^{k=1}(\alpha_{k,\ell m} + \alpha_{k,\ell m}^L \ln v_f)v_f^{k+8}\right), \quad (2.9)$$

where $v_f = (2\pi M f/m)^{1/3}$ and $A_{\ell m}^{\mathrm{PN}}(f)$ is the Padé resummed version of the 3.5 PN (3 PN) amplitude of 22 (33, 44, 21) mode in the Fourier domain (see Appendix A). The Padé resummed version of the PN amplitude was employed to provide a better agreement with the late inspiral part of the hybrid amplitude. The inspiral-merger amplitude is modeled as the product of a Padè resummed PN amplitude and another function that mimics a PN-like expansion. Such a form allows the resulting function to include significantly higher-order terms, thus providing better fits to the late inspiral and merger part of the hybrid amplitude[3] Above, $\alpha_{k,\ell m}$, $\alpha_{k,\ell m}^L$ and $f_{\ell m}^{\mathrm{A}}$ are phenomenological parameters whose values are determined from fits with numerical Fourier transforms of the hybrid waveforms.

---

[3]This idea is similar in spirit to the "factorized resummed amplitude" for effective one-body waveforms proposed by [18].

The ringdown amplitude is modeled from the Fourier transform of a damped sinusoid, which is exponentially damped to mimic the high-frequency fall of the NR waveforms in the Fourier domain. That is,

$$A_{\ell m}^{\mathrm{RD}}(f) = w_{\ell m} e^{-\lambda_{\ell m}} |\mathcal{B}_{\ell m}(f)|, \qquad (2.10)$$

where $\mathcal{B}_{\ell m}(f)$ is the Fourier transform of the $\ell, m, n = 0$ quasinormal mode of a Kerr black hole with mass M_f and dimensionless spin a_f [52], determined from initial masses:

$$\mathcal{B}_{\ell m}(f) = \frac{\sigma_{\ell m} - if}{f_{\ell m}^2 + (\sigma_{\ell m} - if)^2}. \qquad (2.11)$$

The frequencies $f_{\ell m}$ and $\sigma_{\ell m}$ are the real and imaginary parts of the $\ell, m, n = 0$ quasinormal mode frequency $\Omega_{\ell m 0} = 2\pi(f_{\ell m} + i\sigma_{\ell m})$. The phenomenological parameters $\lambda_{\ell m}$ in Eq. (2.10) are determined from fits with numerical Fourier transforms of the hybrid waveforms, while $w_{\ell m}$ is a normalization constant to make the amplitudes continuous at the merger-ringdown matching frequency $f_{\ell m}^{\mathrm{A}}$. The mass M_f

and spin a_f of the final black hole are computed from the masses m_1 and m_2 of the initial black holes, using fitting formulae calibrated to NR simulations. For this work, we use the fitting formulas given by [15].

Our analytical model for the phase of the Fourier domain waveform reads

$$\Psi_{\ell m}(f) = \begin{cases} \Psi_{\ell m}^{\mathrm{IM}}(f); & f < f_{\ell m}^{\mathrm{P}} \\ \Psi_{\ell m}^{\mathrm{RD}}(f); & f \geq f_{\ell m}^{\mathrm{P}} \end{cases}$$

where the phase model for the inspiral-merger part of each mode takes the following form:

$$\Psi_{\ell m}^{\mathrm{IM}}(f) = \Psi_{\ell m}^{\mathrm{PN}}(f) + \sum_{k=0}^{k=4} (\beta_{k,\ell m} + \beta_{k,\ell m}^{\mathrm{L}} \ln v_f$$
$$+ \beta_{k,\ell m}^{\mathrm{L2}} \ln^2 v_f) v_f^{k+8}, \qquad (2.12)$$

where $\Psi_{\ell m}^{\mathrm{PN}}(f)$ is the PN phasing of the ℓm mode, while the higher-order phenomenological coefficients $\beta_{k,\ell m}$, $\beta_{k,\ell m}^{\mathrm{L}}$,
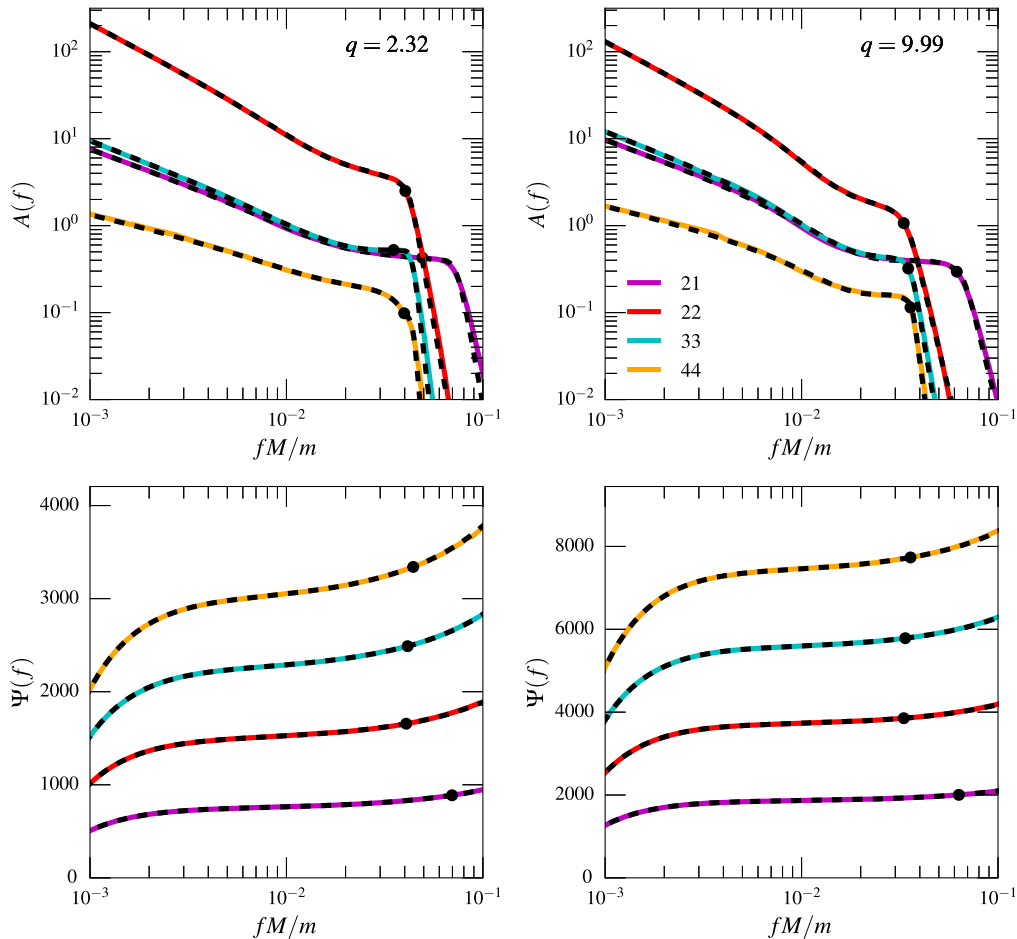

FIG. 1. Comparison between the amplitude (top panels) and phase (bottom panels) of the hybrids and analytical waveforms for selected mass ratios $q = 2.32$ (left panels) and $q = 9.99$ (right panels). In each plot, the solid lines correspond to hybrid waveforms for different modes and the dashed lines correspond to the analytical waveforms for the same mode. The legends show the ℓm value for different modes. The black dots show the transition frequency ($f_{\ell m}^{\mathrm{A}}$ and $f_{\ell m}^{\mathrm{P}}$) from the inspiral-merger to the ringdown part of the phenomenological amplitude and phase models.

$\beta^{\mathrm{L2}}_{k,\ell m}$ are determined from fits against the phase of hybrid waveforms. This particular phenomenological ansatz is motivated from the PN expansion of the frequency domain GW phasing of the inspiral waveforms in the test particle limit (see, e.g., [53]).

For the ringdown part of the phase we simply attach the phase of Fourier transform $\mathcal{B}_{\ell m}(f)$ of the $\ell, m, n = 0$

quasinormal mode at a transition frequency $f^{\mathrm{P}}_{\ell m}$. Thus, our ringdown phase model reads

$$\Psi^{\mathrm{RD}}_{\ell m}(f) = 2\pi f t^{\mathrm{P}}_{\ell m} + \phi^{\mathrm{P}}_{\ell m} + \arctan \mathcal{B}_{\ell m}(f), \qquad (2.13)$$

where $t^{\mathrm{P}}_{\ell m}$ and $\phi^{\mathrm{P}}_{\ell m}$ are computed by matching two phases ($\Psi^{\mathrm{IM}}_{\ell m}$ and $\Psi^{\mathrm{RD}}_{\ell m}$) and their first derivative at the matching
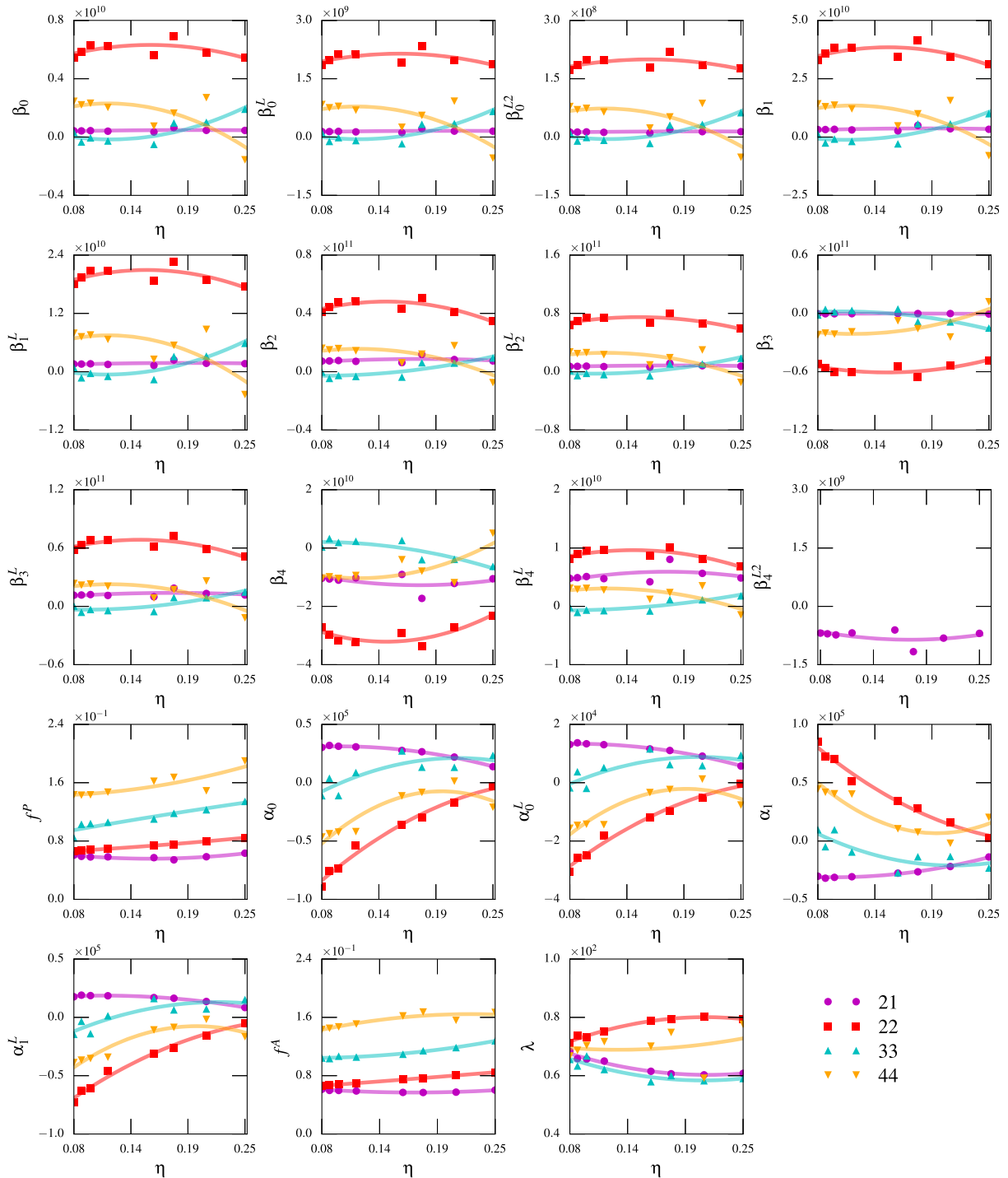

FIG. 2.   The estimated values of the phenomenological parameters describing the analytical waveforms, plotted against the symmetric mass ratio η. Different markers correspond to different modes. Also plotted are the fits given by Eqs. (2.14).
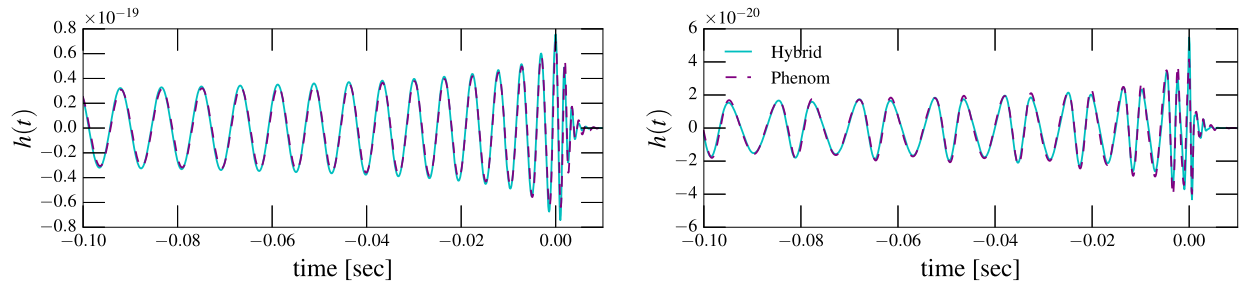
FIG. 3. Comparison between hybrid waveforms and our analytical phenomenological waveforms for a binary with total mass $M = 20M_\odot$ and mass ratio $q = 10$. Hybrid waveforms are constructed using all the modes with $\ell \leq 4$, except the $m = 0$ modes. Phenomenological waveforms are constructed by taking the (discrete) inverse Fourier transform of the analytical waveforms in the Fourier domain. The left panel corresponds to a "face-on" binary (inclination angle $i = 0.00$) while the right panel corresponds to an "edge-on" binary ($i = 1.57$).

frequency $f_{\ell m}^{\mathrm{P}}$. Figure 1 provides a comparison of the amplitude and phase of the numerical Fourier transform of the hybrid waveforms, along with the analytical fits given by Eqs. (2.8) and (2.12).

Finally, the phenomenological parameters describing the analytical model are represented as quadratic functions of the symmetric mass ratio η

$$
\begin{aligned}
\alpha_{i,\ell m} &= a_{i,\ell m} + b_{i,\ell m}\eta + c_{i,\ell m}\eta^2, \\
\alpha_{i,\ell m}^{\mathrm{L}} &= a_{i,\ell m}^{\mathrm{L}} + b_{i,\ell m}^{\mathrm{L}}\eta + c_{i,\ell m}^{\mathrm{L}}\eta^2, \\
\beta_{k,\ell m} &= a_{k,\ell m} + b_{k,\ell m}\eta + c_{k,\ell m}\eta^2, \\
\beta_{k,\ell m}^{\mathrm{L}} &= a_{k,\ell m}^{\mathrm{L}} + b_{k,\ell m}^{\mathrm{L}}\eta + c_{k,\ell m}^{\mathrm{L}}\eta^2, \\
\beta_{j,\ell m}^{\mathrm{L2}} &= a_{j,\ell m}^{\mathrm{L2}} + b_{j,\ell m}^{\mathrm{L2}}\eta + c_{j,\ell m}^{\mathrm{L2}}\eta^2, \\
\lambda_{\ell m} &= a_{\ell m}^{\lambda} + b_{\ell m}^{\lambda}\eta + c_{\ell m}^{\lambda}\eta^2), \\
f_{\ell m}^{\mathrm{A}} &= a_{\ell m}^{\mathrm{A}} + b_{\ell m}^{\mathrm{A}}\eta + c_{\ell m}^{\mathrm{A}}\eta^2)/M, \\
f_{\ell m}^{\mathrm{P}} &= a_{\ell m}^{\mathrm{P}} + b_{\ell m}^{\mathrm{P}}\eta + c_{\ell m}^{\mathrm{P}}\eta^2)/M. \quad (2.14)
\end{aligned}
$$

where the index i runs from 0 to 1, k runs from 0 to 4 and j is 0 except for 21 mode ($j = 0,1$); see supplemental material [60] for numerical values of the parameters. Figure 2 shows the values of the phenomenological parameters estimated from the hybrid waveforms, as well as the fits described by Eq. (2.14).

C. Assessing the accuracy of the analytical model

Here we quantify the faithfulness of the analytical model that we constructed by computing the mismatches of these with the hybrid waveforms, which are assumed as our fiducial waveforms. Indeed, relative contribution of different modes depend on the orientation of the binary with respect to the line of sight. Figure 3 shows some examples of the hybrid waveforms for different orientations along with the corresponding waveforms generated from our analytical model (by taking the inverse Fourier transform). Computation of these polarizations $h_+(t)$ and $h_\times(t)$ is described in Appendix C. Polarizations of the hybrid waveforms have been computed using all the modes up
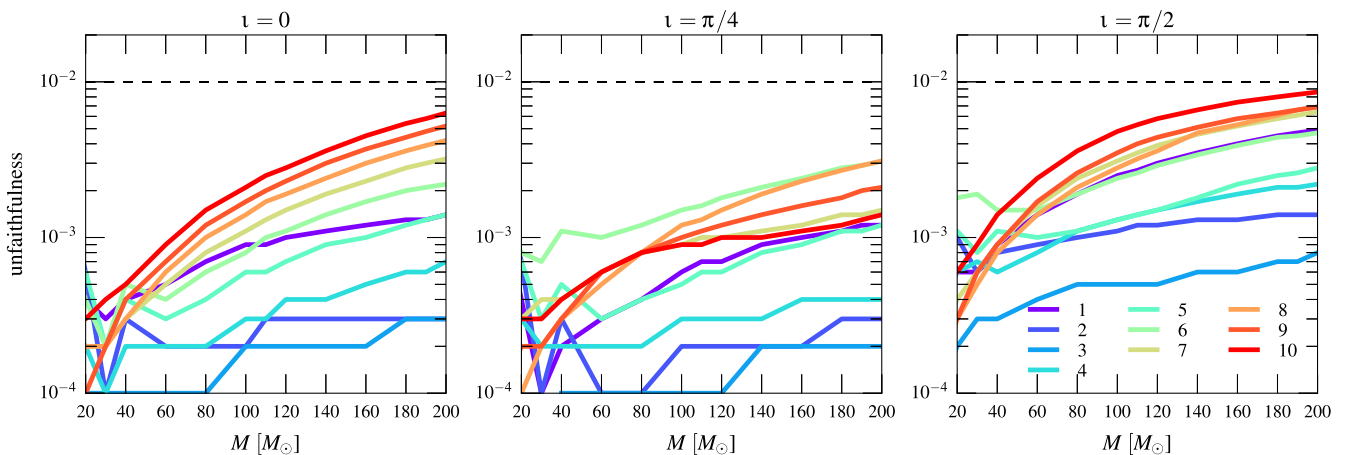

FIG. 4. The unfaithfulness (mismatch) of the analytical waveform family towards hybrids for various inclination angles ι. The horizontal axes report the total mass of the binary and different curves correspond to different mass ratios q (shown in the legend). Horizontal black dashed lines correspond to a mismatch of 1%. The overlaps are computed assuming the design power spectrum of Advanced LIGO (in the "high-power, zero-detuning" configuration [54]), assuming a low-frequency cutoff of 20 Hz.

to $\ell = 4$, except the $m = 0$ modes, see Eq. (C1), while the analytical phenomenological waveforms have been computed using $\ell m = 22, 21, 33, 44$ modes only, by computing the inverse Fourier transform of the expression Eq. (C7) numerically.

Since the relative contribution to the observed $h(t)$ from different modes depend on the relative orientation of the binary, the mismatches of our analytical phenomenological waveforms with the hybrids will be a function of the orientation angles. Figure 4 shows the mismatches for different orientations as a function of the total mass M and mass ratio q of the binary. Relative contribution from subdominant modes are expected to be the smallest [largest] for binaries with inclination angles $\iota = 0$ [$\iota = \pi/2$]. The figure shows that the mismatches are less than 1% for all orientations, illustrating the high faithfulness of our phenomenological waveforms. Note that GW detectors have a strong selection bias towards small inclination angles ($\iota \to 0$). Hence, the mismatches averaged over all orientations are likely to be comparable to the ones reported in the left panel of the Figure ($\iota = 0$).

III. SUMMARY AND CONCLUSIONS

In this paper, we presented an analytical family of frequency-domain waveforms describing the GW signals from nonspinning black-hole binaries, including some of the leading subdominant modes of the radiation ($\ell m = 21, 33, 44$), apart from the dominant ($\ell m = 22$) mode. The construction of these analytical waveforms involves two major steps: 1) the construction of a set of hybrid waveforms by combining the spherical harmonic modes of PN and NR waveforms corresponding to a limited set of mass ratios $1 \leq q \leq 10$, 2) representing the numerical Fourier transform of the hybrid waveforms by a suitable set of analytical functions which allow us to interpolate these waveforms smoothly over the parameter space. The analytical gravitational waveforms that are constructed in this way are highly faithful (mismatch 0.01%–1%) to our target hybrid waveforms that include all the modes up to $\ell = 4$ (except the $m = 0$ modes).

The Fourier domain amplitude of our phenomenological waveforms contain a inspiral-merger part that is smoothly matched to the ringdown part. The inspiral-merger amplitude is modeled as the product of a Padè resummed version of the Fourier domain PN amplitude and another function that mimics a PN-like expansion whose coefficients are determined by fitting against the Fourier-domain amplitude of the hybrid waveforms. The ringdown part is modeled as the Fourier transform of a time-symmetric damped sinusoid, which is exponentially damped to mimic the high-frequency fall of the NR waveforms in Fourier domain. Similarly, the Fourier domain phase is modeled as a PN-like series including the known coefficients from PN theory till 3.5PN order, while the higher-order "pseudo-PN" terms are determined by fitting against the hybrid

waveforms. The resulting waveforms are also computationally inexpensive to generate, allowing their direct implementation in GW searches and parameter estimation.

A note on the limitations of this work: These waveforms aim to model the GW signals from nonspinning black-hole binaries in quasicircular orbits. Spin effects of black holes are not considered. (We note that, an approximate phenomenological model for spinning binaries, making use of rescaled amplitudes and frequencies of the $\ell = m = 2$ mode for modeling the nonquadrupole modes has been developed recently [42] and an EOB model is under development [55]). Additionally, we consider only a subset of the subdominant modes $\ell m = 21, 33, 44$. Although the subdominant modes that we neglect here makes no appreciable contributions to the total signal for the mass ratios that we consider, this may not be the case for even higher mass ratios. Modeling of some of the subdominant modes (e.g., $\ell m = 32, 43$, etc.) that we neglect here could be harder, due to the effect of "mode-mixing" [56]. There is ongoing work that aims to include the spin effects, to model the subdominant modes that are neglected here, and to extend the validity of these waveforms making use of numerical waveforms modeling binary black holes with extreme mass ratios.

APPENDIX A: PADÉ SUMMATION ON THE POST-NEWTONIAN AMPLITUDE IN THE FOURIER DOMAIN

The PN expression for various mode amplitudes have a stationary point at high frequencies when higher-order PN corrections are included. This makes it inconvenient to model the amplitude of the phenomenological waveforms as a factorized correction to the PN waveforms as shown in
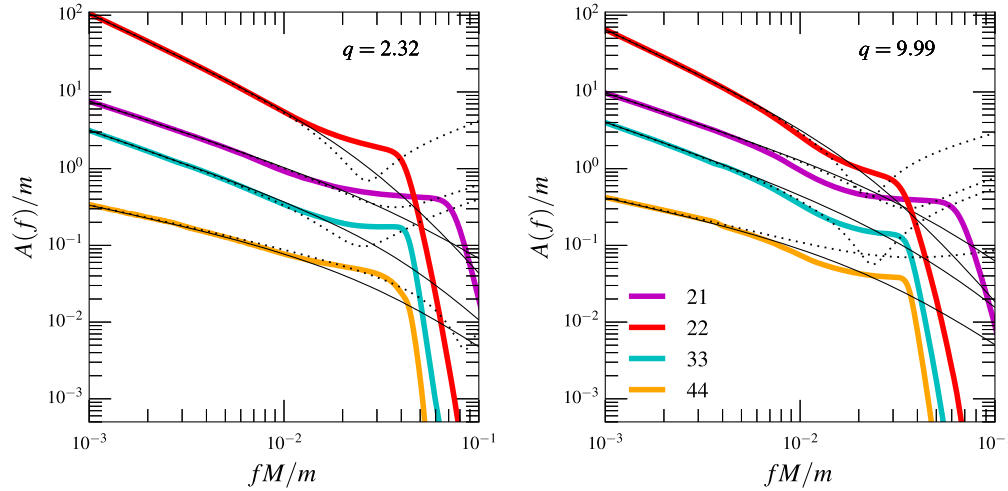
FIG. 5. Comparison of the Padé approximant of the PN inspiral amplitude (thin, solid lines) with regular Taylor expanded amplitude (thin, dotted lines) and the amplitude of the hybrid waveform (thick, solid lines) for different modes $\ell m = 21, 22, 33, 44$. The left panel corresponds to mass ratio $q = 2.32$ while the right panel corresponds to mass ratio $q \simeq 10$.

Eq. (2.9). In order to resolve this issue, and to generally improve the agreement of PN amplitude with that of the hybrid waveforms, we construct our inspiral amplitude model by performing Padé summation of these expressions. Padé summation of a given function involves finding a suitable rational function whose Taylor expansion to a given order matches exactly with the Taylor expression of the original function to the same order. For instance, Padé summation of a simple power series $\sum_{k=0}^{n} a_n x^n$ can be written as

$$P_q^p(x) = \frac{\sum_{k=0}^{p} b_k x^k}{\sum_{k=0}^{q} c_k x^k}, \tag{A1}$$

where $p + q = n$. Each of these coefficients (b_k and c_k) then can readily be obtained by demanding that a Taylor expansion of the above to order n reproduces exactly the first n terms the given power series. Such rational functions are called Padé approximants (see Appendix A of Ref. [57] for a related discussion).

After comparing various Padé approximants corresponding to PN amplitude expressions for each mode we find the most suitable (i.e., an approximant with no point of inflection) approximant corresponds to the choice of rational functions associated with $p = 0$ and $q = n$, i.e., P_n^0. For instance for the $\ell = m = 2$ mode whose (normalized) amplitude is given by the series, $\sum_{k=0}^{7} \alpha_k v^k$, the Padé approximant we find most suitable for our purposes is given by

$$P_7^0(v) = \frac{\beta_0}{\sum_{k=0}^{7} \gamma_k v^k}. \tag{A2}$$

Moreover by the virtue of the use of normalized amplitude expressions in constructing the Padé approximants we can

choose (without any loss of generality), $\beta_0 = \gamma_0 = 1$, which leads to the following simple expression

$$P_7^0(v) = \frac{1}{1 + \sum_{k=1}^{7} \gamma_k v^k}. \tag{A3}$$

Figure 5 shows a comparison of the standard Taylor expanded 3.5 PN (3 PN) amplitude for 22 (21, 33, 44) with our corresponding resummed Padé function as well as the amplitude of the hybrid waveform in the Fourier domain. Explicit expressions for Padé approximants for modes we consider here are listed in Appendix B below.

APPENDIX B: PADÉ RESUMMED FREQUENCY DOMAIN EXPRESSIONS FOR THE INSPIRAL AMPLITUDE

As discussed above, occurrence of divergences in the PN amplitudes when including higher PN terms motivates us to find Padé resummed expressions of the PN amplitudes as our inspiral amplitude model. Here we provide, analytical expression for the complete inspiral model for each mode in the frequency domain which are constructed using the prescription listed in Ref. [58] and uses stationary phase approximation. Resulting expression for each mode of the gravitational wave polarizations in the frequency domain take the following general form

$$\tilde{h}_{\ell m}(f) = \frac{M^2}{D_L} \pi \sqrt{\frac{2\eta}{3}} v_f^{-7/2} e^{-im\Psi(v_f)} H_{\ell m}(v_f). \tag{B1}$$

Here, M and η again denote the total mass and symmetric mass ratio parameter of the binary whereas D_L is the luminosity distance of the source. The quantity v_f is given by $v_f \equiv (2\pi M f/m)^{1/3}$ and $\Psi(v_f)$ represents the orbital

phase of the binary computed using stationary phase approximation (see, for instance, Ref. [58] for a related discussion). Finally, $H_{\ell m}$ are the Padé resummed version of the inspiral amplitudes and takes following form for the modes whose complete models are presented in this study. They read

$$H_{22} = {}^{22}P_7^0(v_f) \tag{B2a}$$

$$H_{21} = i\frac{\sqrt{2}}{3}\delta[{}^{21}P_5^0(v_f)]v_f \tag{B2b}$$

$$H_{33} = -i\frac{3}{4}\sqrt{\frac{5}{7}}\delta[{}^{33}P_5^0(v_f)]v_f \tag{B2c}$$

$$H_{44} = -\frac{4}{9}\sqrt{\frac{10}{7}}(1-3\eta)[{}^{44}P_4^0(v_f)]v_f^2 \tag{B2d}$$

here, ${}^{\ell m}P_n^0(v_f)$ are Padé resummed expressions for (normalized) inspiral amplitudes corresponding to $p=0$ and $q=n$ (see Appendix A for related discussions) and can be expressed in the following general form:

$$^{\ell m}P_n^0(v) = \frac{1}{1 + \sum_{k=1}^{n}\gamma_k^{\ell m}v^k}, \tag{B3}$$

where $\gamma^{\ell m}$ corresponding to each mode can be written in the following form,

$$\gamma_1^{22} = 0 \tag{B4a}$$

$$\gamma_2^{22} = \frac{323}{224} - \frac{451}{168}\eta \tag{B4b}$$

$$\gamma_3^{22} = 0 \tag{B4c}$$

$$\gamma_4^{22} = \frac{44213383}{8128512} - \frac{92437}{48384}\eta + \frac{483509}{169344}\eta^2 \tag{B4d}$$

$$\gamma_5^{22} = \frac{85\pi}{64} + \left(24\,i - \frac{85\pi}{16}\right)\eta \tag{B4e}$$

$$\gamma_6^{22} = \frac{40919017211}{1226244096} - \frac{428\,i\pi}{105} + \left(-\frac{1906061676931}{15021490176}\right.$$
$$\left. + \frac{205\pi^2}{48}\right)\eta + \frac{6864704395}{1251790848}\eta^2 - \frac{48013667}{34771968}\eta^3 \tag{B4f}$$

$$\gamma_7^{22} = \frac{633281\pi}{1161216} + \left(\frac{2357\,i}{324} - \frac{21367\pi}{3456}\right)\eta$$
$$+ \left(-\frac{86519\,i}{945} + \frac{496409\pi}{24192}\right)\eta^2 \tag{B4g}$$

$$\gamma_1^{21} = 0 \tag{B4h}$$

$$\gamma_2^{21} = -\frac{335}{672} - \frac{117}{56}\eta \tag{B4i}$$

$$\gamma_3^{21} = \frac{i}{2} + \pi + 2\,i\,\ln 2 \tag{B4j}$$

$$\gamma_4^{21} = \frac{2984407}{8128512} + \frac{62659}{12544}\eta + \frac{96847}{56448}\eta^2 \tag{B4k}$$

$$\gamma_5^{21} = -\frac{335\,i}{1344} + \frac{1115\pi}{1344} + \eta\left(\frac{1255\,i}{112} - \frac{885\pi}{112} - \frac{145}{28}i\,\ln 2\right)$$
$$-\frac{335}{336}i\,\ln 2 \tag{B4l}$$

$$\gamma_1^{33} = 0 \tag{B4m}$$

$$\gamma_2^{33} = \frac{1945}{672} - \frac{27}{8}\eta \tag{B4n}$$

$$\gamma_3^{33} = \frac{2\,i}{5} - \pi + 6\,i\,\ln 2 - 6\,i\,\ln 3 \tag{B4o}$$

$$\gamma_4^{33} = \frac{4822859617}{447068160} - \frac{5571877}{887040}\eta + \frac{301321}{63360}\eta^2 \tag{B4p}$$

$$\gamma_5^{33} = \frac{389\,i}{32} - \frac{2105\pi}{1344} - \frac{1945\,i}{112}\ln(3/2)$$
$$+ \eta\left(\frac{33079\,i}{1944} - \frac{23\pi}{16} + \frac{93\,i}{4}\ln(3/2)\right) \tag{B4q}$$

$$\gamma_1^{44} = 0 \tag{B4r}$$

$$\gamma_2^{44} = \frac{1}{1-3\eta}\left(-\frac{158383}{36960} + \frac{128221}{7392}\eta - \frac{1063}{88}\eta^2\right) \tag{B4s}$$

$$\gamma_3^{44} = \frac{1}{1-3\eta}\left(-\frac{42\,i}{5} + 2\pi + \eta\left(\frac{1193\,i}{40} - 6\pi - 24\,i\,\ln 2\right)\right.$$
$$\left. + 8\,i\,\ln 2\right) \tag{B4t}$$

$$\gamma_4^{44} = \frac{1}{(1-3\eta)^2}\left(\frac{5783159561419}{319653734400} - \frac{6510652977943}{53275622400}\eta\right.$$
$$+ \frac{8854729392203}{35517081600}\eta^2 - \frac{1326276157}{8456448}\eta^3$$
$$\left. + \frac{63224063}{1006720}\eta^4\right). \tag{B4u}$$

Finally, the orbital phase takes the following form in Fourier domain

$$\Psi(v_f) = 2\pi f t_0 - \pi/4 + \frac{3}{256\eta v_f^5}\left[\sum_{k=0}^{7}\psi_k v_f^k\right], \tag{B5}$$

where, t_0 represents a reference time[4] and ψ_k denote the PN corrections to the leading-order orbital phase. These read

$$\psi_0 = 1, \tag{B6a}$$

$$\psi_1 = 0, \tag{B6b}$$

$$\psi_2 = \frac{3715}{756} + \frac{55}{9}\eta, \tag{B6c}$$

$$\psi_3 = -16\pi, \tag{B6d}$$

$$\psi_4 = \frac{15293365}{508032} + \frac{27145}{504}\eta + \frac{3085}{72}\eta^2, \tag{B6e}$$

$$\psi_5 = \pi\left(\frac{38645}{756} - \frac{65}{9}\eta\right)(1 + 3\ln v_f), \tag{B6f}$$

$$\psi_6 = \frac{11583231236531}{4694215680} - \frac{6848\gamma_E}{21} - \frac{640\pi^2}{3}$$
$$+ \left(-\frac{15737765635}{3048192} + \frac{2255\pi^2}{12}\right)\eta$$
$$+ \frac{76055}{1728}\eta^2 - \frac{127825}{1296}\eta^3 - \frac{6848}{21}\ln(4v_f), \tag{B6g}$$

$$\psi_7 = \frac{77096675\pi}{254016} + \frac{378515\pi}{1512}\eta - \frac{74045\pi}{756}\eta^2, \tag{B6h}$$

where γ_E is the Euler's constant.

APPENDIX C: COMPUTING THE + and × POLARIZATION WAVEFORMS FROM THE SPHERICAL HARMONIC MODES IN THE FREQUENCY DOMAIN

The complex time series, $\mathfrak{h} = h_+ - ih_\times$, can be decomposed into a sum of spherical harmonic modes as

$$\mathfrak{h}(t) = \sum_{\ell=2}^{+\infty} \sum_{m=-\ell}^{\ell} \mathfrak{h}_{\ell m}(t) Y_{-2}^{\ell m}(\iota, \varphi_0), \tag{C1}$$

where $Y_{-2}^{\ell m}$'s (the spin-weighted spherical harmonics of weight -2) are functions of the spherical angles (ι, φ_0) defining the binary's orientation and are given as

$$Y_{-2}^{\ell m} = \sqrt{\frac{2\ell+1}{4\pi}} d_2^{\ell m}(\iota) e^{im\varphi_0}, \tag{C2}$$

and where $d_2^{\ell m}(\iota)$ are the Wigner d functions (e.g., [59]). The spherical harmonic modes of the waveform in time domain have the following generic form:

$$\mathfrak{h}_{\ell m}(t) = A_{\ell m}(t) e^{i\varphi_{\ell m}(t)} \tag{C3}$$

Further, $m < 0$ modes are related to $m > 0$ modes as $\mathfrak{h}_{\ell,-m}(t) = (-)^\ell \mathfrak{h}_{\ell m}^*(t)$ [43]. Using Eq. (C2) and Eq. (C3) in Eq. (C1) and making use of the above property, we can write expressions for the real and imaginary part as

$$h_+(t) = \sum_{\ell=2}^{+\infty} \sum_{m=1}^{\ell} \sqrt{\frac{2\ell+1}{4\pi}} [(-)^\ell d_2^{\ell,-m}(\iota) + d_2^{\ell m}(\iota)] A_{\ell m}(t) \cos[\varphi_{\ell m}(t) + m\varphi_0], \tag{C4a}$$

$$h_\times(t) = \sum_{\ell=2}^{+\infty} \sum_{m=1}^{\ell} \sqrt{\frac{2\ell+1}{4\pi}} [(-)^\ell d_2^{\ell,-m}(\iota) - d_2^{\ell m}(\iota)] A_{\ell m}(t) \sin[\varphi_{\ell m}(t) + m\varphi_0]. \tag{C4b}$$

The frequency domain + and × waveforms can now be obtained simply by taking the Fourier transform of $h_+(t)$ and $h_\times(t)$, respectively,

$$\tilde{h}_+(f) = \sum_{\ell=2}^{+\infty} \sum_{m=1}^{\ell} \sqrt{\frac{2\ell+1}{4\pi}} [(-)^\ell d_2^{\ell,-m}(\iota) + d_2^{\ell m}(\iota)]\{\cos(m\varphi_0)\tilde{h}_{\ell m}^R(f) - \sin(m\varphi_0)\tilde{h}_{\ell m}^I(f)\}, \tag{C5a}$$

$$\tilde{h}_\times(f) = \sum_{\ell=2}^{+\infty} \sum_{m=1}^{\ell} \sqrt{\frac{2\ell+1}{4\pi}} [(-)^\ell d_2^{\ell,-m}(\iota) - d_2^{\ell m}(\iota)]\{\sin(m\varphi_0)\tilde{h}_{\ell m}^R(f) + \cos(m\varphi_0)\tilde{h}_{\ell m}^I(f)\}. \tag{C5b}$$

where $\tilde{h}_{\ell m}^R(f)$ and $\tilde{h}_{\ell m}^I(f)$ are the Fourier transforms of the real and imaginary parts of $\mathfrak{h}_{\ell m}(t)$.

---

[4]Note that we have set the phase at reference time to zero, since phase shifts can be introduced on the waveform by the spherical harmonic basis functions; see Eq. (C7).

$$\tilde{h}_{\ell m}^{R}(f) = \int_{-\infty}^{\infty} e^{2\pi i f t} A_{\ell m}(t) \cos\varphi_{\ell m}(t) dt, \qquad \text{(C6a)}$$

$$\tilde{h}_{\ell m}^{I}(f) = \int_{-\infty}^{\infty} e^{2\pi i f t} A_{\ell m}(t) \sin\varphi_{\ell m}(t) dt. \qquad \text{(C6b)}$$

We know that for nonspinning binaries (as well as for nonprecessing binaries), $\tilde{h}_{\ell m}^{I}(f) = -i\tilde{h}_{\ell m}^{R}(f)$. This allows us to write Eq. (C5) as

$$\tilde{h}_{+}(f) = \sum_{\ell=2}^{+\infty} \sum_{m=1}^{\ell} \left[(-)^{\ell} \frac{d_{2}^{\ell,-m}(\iota)}{d_{2}^{\ell m}(\iota)} + 1 \right] Y_{-2}^{\ell m}(\iota, \varphi_0) \tilde{h}_{\ell m}^{R}(f)$$

$$\text{(C7a)}$$

$$\tilde{h}_{\times}(f) = -i \sum_{\ell=2}^{+\infty} \sum_{m=1}^{\ell} \left[(-)^{\ell} \frac{d_{2}^{\ell,-m}(\iota)}{d_{2}^{\ell m}(\iota)} - 1 \right] Y_{-2}^{\ell m}(\iota, \varphi_0) \tilde{h}_{\ell m}^{R}(f).$$

$$\text{(C7b)}$$

Note that $\tilde{h}_{\ell m}^{R}(f)$ can be written as

$$\tilde{h}_{\ell m}^{R}(f) = A_{\ell m}(f) e^{i\Psi_{\ell m}(f)}. \qquad \text{(C8)}$$

The phenomenological model for the frequency domain amplitudes $A_{\ell m}(f)$ and phases $\Psi_{\ell m}(f)$ are obtained by fitting the FFT of hybrids.

The signal observed at a detector is a linear combination of the two polarizations h_+ and $h_\times$. The Fourier transform of the observed signal can be written in terms of the Fourier transform of the two polarizations as

$$\tilde{h}(f) = F_{+}(\theta, \phi, \psi)\tilde{h}_{+}(f) + F_{\times}(\theta, \phi, \psi)\tilde{h}_{\times}(f), \qquad \text{(C9)}$$

where the antenna pattern functions $F_{+}(\theta, \phi, \psi)$ and $F_{\times}(\theta, \phi, \psi)$ are functions of two angles (θ, ϕ) describing the location of the binary in the sky and the polarization angle ψ.

[1] B. P. Abbott *et al.* (LIGO Scientific and Virgo Collaborations), Phys. Rev. Lett. **116**, 061102 (2016).

[2] B. P. Abbott *et al.* (LIGO Scientific and Virgo Collaborations), Phys. Rev. Lett. **116**, 241103 (2016).

[3] B. P. Abbott *et al.* (LIGO Scientific and Virgo Collaboration), Phys. Rev. Lett. **118**, 221101 (2017).

[4] B. P. Abbott *et al.* (LIGO Scientific Collaboration), Astrophys. J. Lett. **833**, L1 (2016).

[5] B. P. Abbott *et al.* (LIGO Scientific and Virgo Collaborations), Phys. Rev. X **6**, 041015 (2016).

[6] S. A. Usman *et al.*, Classical Quantum Gravity **33**, 215004 (2016).

[7] C. Messick, K. Blackburn, P. Brady, P. Brockill, K. Cannon, R. Cariou, S. Caudill, S. J. Chamberlin, J. D. E. Creighton, R. Everett *et al.*, Phys. Rev. D **95**, 042001 (2017).

[8] J. Veitch *et al.*, Phys. Rev. D **91**, 042003 (2015).

[9] B. P. Abbott *et al.* (LIGO Scientific and Virgo Collaborations), Phys. Rev. Lett. **116**, 221101 (2016).

[10] A. Buonanno and T. Damour, Phys. Rev. D **59**, 084006 (1999).

[11] A. Buonanno and T. Damour, Phys. Rev. D **62**, 064015 (2000).

[12] A. Taracchini *et al.*, Phys. Rev. D **89**, 061502 (2014).

[13] A. Bohé *et al.*, Phys. Rev. D **95**, 044028 (2017).

[14] Y. Pan, A. Buonanno, R. Fujita, E. Racine, and H. Tagoshi, Phys. Rev. D **83**, 064003 (2011); **87**, 109901(E) (2013).

[15] Y. Pan, A. Buonanno, M. Boyle, L. T. Buchman, L. E. Kidder, H. P. Pfeiffer, and M. A. Scheel, Phys. Rev. D **84**, 124052 (2011).

[16] Y. Pan, A. Buonanno, A. Taracchini, L. E. Kidder, A. H. Mroué, H. P. Pfeiffer, M. A. Scheel, and B. Szilágyi, Phys. Rev. D **89**, 084006 (2014).

[17] T. Damour and A. Nagar, Phys. Rev. D **79**, 081503 (2009).

[18] T. Damour, B. R. Iyer, and A. Nagar, Phys. Rev. D **79**, 064004 (2009).

[19] T. Damour, A. Nagar, and S. Bernuzzi, Phys. Rev. D **87**, 084035 (2013).

[20] P. Ajith *et al.*, Phys. Rev. D **77**, 104017 (2008).

[21] P. Ajith, M. Hannam, S. Husa, Y. Chen, B. Brügmann, N. Dorband, D. Müller, F. Ohme, D. Pollney, C. Reisswig *et al.*, Phys. Rev. Lett. **106**, 241101 (2011).

[22] L. Santamaria *et al.*, Phys. Rev. D **82**, 064016 (2010).

[23] M. Hannam, P. Schmidt, A. Bohé, L. Haegel, S. Husa, F. Ohme, G. Pratten, and M. Pürrer, Phys. Rev. Lett. **113**, 151101 (2014).

[24] S. Khan, S. Husa, M. Hannam, F. Ohme, M. Pürrer, X. J. Forteza, and A. Bohé, Phys. Rev. D **93**, 044007 (2016).

[25] S. Husa, S. Khan, M. Hannam, M. Pürrer, F. Ohme, X. J. Forteza, and A. Bohé, Phys. Rev. D **93**, 044006 (2016).

[26] B. P. Abbott *et al.* (Virgo and LIGO Scientific Collaborations), Classical Quantum Gravity **34**, 104002 (2017).

[27] V. Varma, P. Ajith, S. Husa, J. C. Bustillo, M. Hannam, and M. Pürrer, Phys. Rev. D **90**, 124004 (2014).

[28] J. Calderón Bustillo, S. Husa, A. M. Sintes, and M. Pürrer, Phys. Rev. D **93**, 084019 (2016).

[29] V. Varma and P. Ajith, arXiv:1612.05608.

[30] A. M. Sintes and A. Vecchio, in *Proceedings, 34th Rencontres de Moriond gravitational waves and experimental gravity: Les Arcs, France, 1999* (2000), p. 73, arXiv: gr-qc/0005058, http://alice.cern.ch/format/showfull?sysnb= 2187848.

[31] C. Van Den Broeck and A. S. Sengupta, Classical Quantum Gravity **24**, 1089 (2007).

[32] K. Arun, B. R. Iyer, B. Sathyaprakash, S. Sinha, and C. V. D. Broeck, Phys. Rev. D **76**, 104016 (2007).

[33] M. Trias and A. M. Sintes, Classical Quantum Gravity **25**, 184032 (2008).

[34] K. G. Arun *et al.*, Classical Quantum Gravity **26**, 094027 (2009).

[35] P. B. Graff, A. Buonanno, and B. S. Sathyaprakash, Phys. Rev. D **92**, 022002 (2015).

[36] J. Lange *et al.*, Phys. Rev. D **96**, 104041 (2017).

[37] R. O'Shaughnessy, J. Blackman, and S. E. Field, Classical Quantum Gravity **34**, 144002 (2017).

[38] C. K. Mishra, K. G. Arun, B. R. Iyer, and B. S. Sathyaprakash, Phys. Rev. D **82**, 064010 (2010).

[39] N. V. Krishnendu, K. G. Arun, and C. K. Mishra, Phys. Rev. Lett. **119**, 091101 (2017).

[40] P. Ajith *et al.*, Classical Quantum Gravity **24**, S689 (2007).

[41] P. Ajith, Classical Quantum Gravity **25**, 114033 (2008).

[42] L. London *et al.*, Report No. LIGO-P1700203-v2.

[43] L. E. Kidder, Phys. Rev. D **77**, 044016 (2008).

[44] M. Favata, Classical Quantum Gravity **27**, 084036 (2010).

[45] D. Pollney and C. Reisswig, Astrophys. J. **732**, L13 (2011).

[46] G. Faye, S. Marsat, L. Blanchet, and B. R. Iyer, Classical Quantum Gravity **29**, 175004 (2012).

[47] L. Blanchet, G. Faye, B. R. Iyer, and S. Sinha, Classical Quantum Gravity **25**, 165003 (2008).

[48] K. G. Arun, L. Blanchet, B. R. Iyer, and M. S. S. Qusailah, Classical Quantum Gravity **21**, 3771 (2004); **22**, 3115(E) (2005).

[49] L. Blanchet, B. R. Iyer, C. M. Will, and A. G. Wiseman, Classical Quantum Gravity **13**, 575 (1996).

[50] L. Blanchet, T. Damour, G. Esposito-Farese, and B. R. Iyer, Phys. Rev. Lett. **93**, 091101 (2004).

[51] J. Calderón Bustillo, A. Bohé, S. Husa, A. M. Sintes, M. Hannam, and M. Pürrer, arXiv:1501.00918.

[52] E. Berti, V. Cardoso, and A. O. Starinets, Classical Quantum Gravity **26**, 163001 (2009).

[53] V. Varma, R. Fujita, A. Choudhary, and B. R. Iyer, Phys. Rev. D **88**, 024038 (2013).

[54] Advanced LIGO anticipated sensitivity curves, Report No. LIGO T0900288-v3, URL https://dcc.ligo.org/LIGO-T0900288/public.

[55] R. Cotesta *et al.* (to be published).

[56] E. Berti and A. Klein, Phys. Rev. D **90**, 064012 (2014).

[57] T. Damour, B. R. Iyer, and B. S. Sathyaprakash, Phys. Rev. D **57**, 885 (1998).

[58] C. Van Den Broeck and A. S. Sengupta, Classical Quantum Gravity **24**, 155 (2007).

[59] Y. Wiaux, L. Jacques, and P. Vandergheynst, J. Comput. Phys. **226**, 2359 (2007).

[60] See Supplemental Material at http://link.aps.org/supplemental/10.1103/PhysRevD.96.124010 for numerical values of the phenomenological parameters.